Exp. Theo. NANOTECHNOLOGY 9 (2025) 347-360 https://doi.org/10.56053/9.2.347

Structural and optical investigations of SnO_2 nanowires

*A. Tony, R. Clarison**

Materials Division, Heriot-Watt University, Edinburgh, Scotland, UK
Email: Clari@hw.ac.uk

Received 15/12/2024, *Received in revised form* 12/2/2025, *Accepted* 9/3/2025, *Published* 15/4/2025

In this study, SnO_2 nanowires and Sb nanoparticles were synthesized using $SnCl_4 \cdot 5H_2O$ and $SbCl_3$ dissolved in acetone. The resulting solution was deposited onto a glass substrate via spray pyrolysis. XRD analysis confirmed that the resulting film was polycrystalline with a tetragonal crystal structure. FESEM imaging revealed a nanowire morphology for SnO_2 and nanoparticle morphology for Sb. EDX analysis showed that increasing the Sb concentration led to a decrease in SnO_2 content, from 72% to 68% by weight. The optical properties were thoroughly investigated using a UV-VIS spectrophotometer, revealing that absorbance, reflectance, and extinction coefficient increased with higher Sb content. Meanwhile, both the energy bandgap and refractive index decreased with increasing Sb content, from 3.92 to 3.80 eV and from 2.24 to 2.22, respectively. These properties suggest that the films are well-suited for nanoelectronic applications, due to their tunability through compositional adjustment and their unique nanostructure—where Sb nanoparticles adhere to SnO_2 nanowires—enhancing their potential for use in sensing devices.

Keywords: SnO_2; Nanowires; Spray pyrolysis.

1. INTRODUCTION

Due to their exceptional physical and chemical properties, nanomaterials have garnered significant attention from researchers across various scientific fields. In particular, metal oxide semiconductors have recently become a focal point of study because of their unique structural and optical characteristics [1, 2]. Among these, tin dioxide (SnO_2) stands out as a prominent material [3]. SnO_2 possesses a wide bandgap of approximately 3.7 eV and exhibits a rutile crystal structure, making it highly suitable for a range of applications including lithium-ion batteries [4], gas sensors [5], optoelectronic devices [6], and transparent conducting electrodes [7]. Various nanostructures of SnO_2 have been extensively investigated, demonstrating excellent thermal stability and optical conductivity [8, 9].

Incorporating antimony (Sb) into SnO_2 has led to the development of nanocomposites with enhanced optical and structural properties, which are highly effective in applications such as photodetectors, liquid crystal displays, touchscreens, solar cells, and low-emission glass [10–13]. Sb doping improves electrical conductivity and increases visible light absorption in SnO_2 [14]. Various deposition techniques have been employed to synthesize Sb-doped SnO_2 films, including sputtering, chemical vapor deposition, spray pyrolysis, sol-gel processing, and electron beam evaporation [15–19]. Among these, spray pyrolysis stands out as a particularly advantageous method due to its simplicity, cost-effectiveness, and ability to produce thin films with high crystallinity and uniformity [20, 21].

This study aims to synthesize Sb-doped SnO_2 films featuring a nanoparticle-on-nanowire structure using the spray pyrolysis technique, with a focus on optimizing their optical properties for targeted applications.

2. EXPERIMENTAL

Prior to the deposition process, glass substrates were cleaned by immersing them in an ultrasonic bath containing ethanol for 10 minutes, followed by rinsing with deionized water and drying using nitrogen gas. Subsequently, a 0.1 M solution of $SnCl_4{\cdot}5H_2O$ was prepared by dissolving it in 100 mL of acetone and stirring the mixture on a magnetic stirrer at 35 °C for 20 minutes. Similarly, for Sb doping, a 0.1 M solution of $SbCl_3$ was also prepared in 100 mL of acetone and stirred under the same conditions.

Spray pyrolysis was employed to deposit both pure $SnCl_4{\cdot}5H_2O$ and Sb-doped $SnCl_4{\cdot}5H_2O$ with varying Sb concentrations (1, 3, 5, and 7 wt%). The prepared solutions were introduced into the spray pyrolysis system, where the glass substrate was placed on a heated plate and allowed to reach the optimal deposition temperature of 350 °C [23]. The spraying was conducted using nitrogen gas at a pressure of 3 bar. The nozzle-to-substrate distance was maintained at 25 cm. Each spray cycle lasted 7 seconds, with an interval of 75 seconds between successive sprays to ensure complete nucleation and stabilization of the film on the substrate at a consistent temperature.

Characterization of the films was carried out using a Field Emission Scanning Electron Microscope (FESEM) and Energy Dispersive X-ray spectroscopy (EDX), both from TESCAN (Czech Republic). X-ray diffraction (XRD) analysis was performed using a SHIMADZU 6000 instrument with a Cu Kα radiation source ($\lambda = 0.154$ nm). Optical properties were investigated using a SHIMADZU UV-VIS spectrophotometer.

3. RESULTS AND DISCUSSION

The crystal structures of pure SnO_2 and Sb-doped SnO_2 were analyzed using an X-ray diffractometer, as illustrated in Figure 1. The diffraction patterns confirm the presence of SnO_2, while the intensity of the SnO_2 peaks decreases with increasing Sb content, indicating the incorporation of Sb into the SnO_2 matrix. The patterns reveal a polycrystalline structure with prominent diffraction planes corresponding to (110), (101), (200), and (211), located at 2θ values of 26.6°, 33.9°, 37.9°, and 51.8°, respectively. These results are consistent with the standard JCPDS card No. 041-1445 and align with previously reported data [24].

Figure 2 provides further evidence of the successful doping of SnO_2 nanowires with Sb nanoparticles. The image shows well-defined nanowires with an average width ranging from 90 to 280 nm, lengths of approximately 10 microns, and an average diameter of about 87 nm. Additionally, Sb nanoparticles are visibly attached to the surfaces of the SnO_2 nanowires, with an average particle size of around 75 nm.

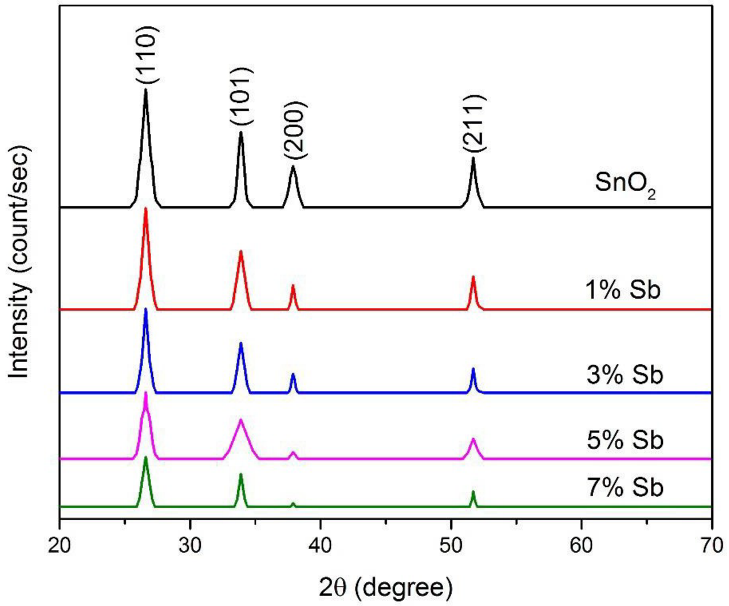

Figure 1 XRD patterns of SnO_2 and different Sb contents doped SnO_2.

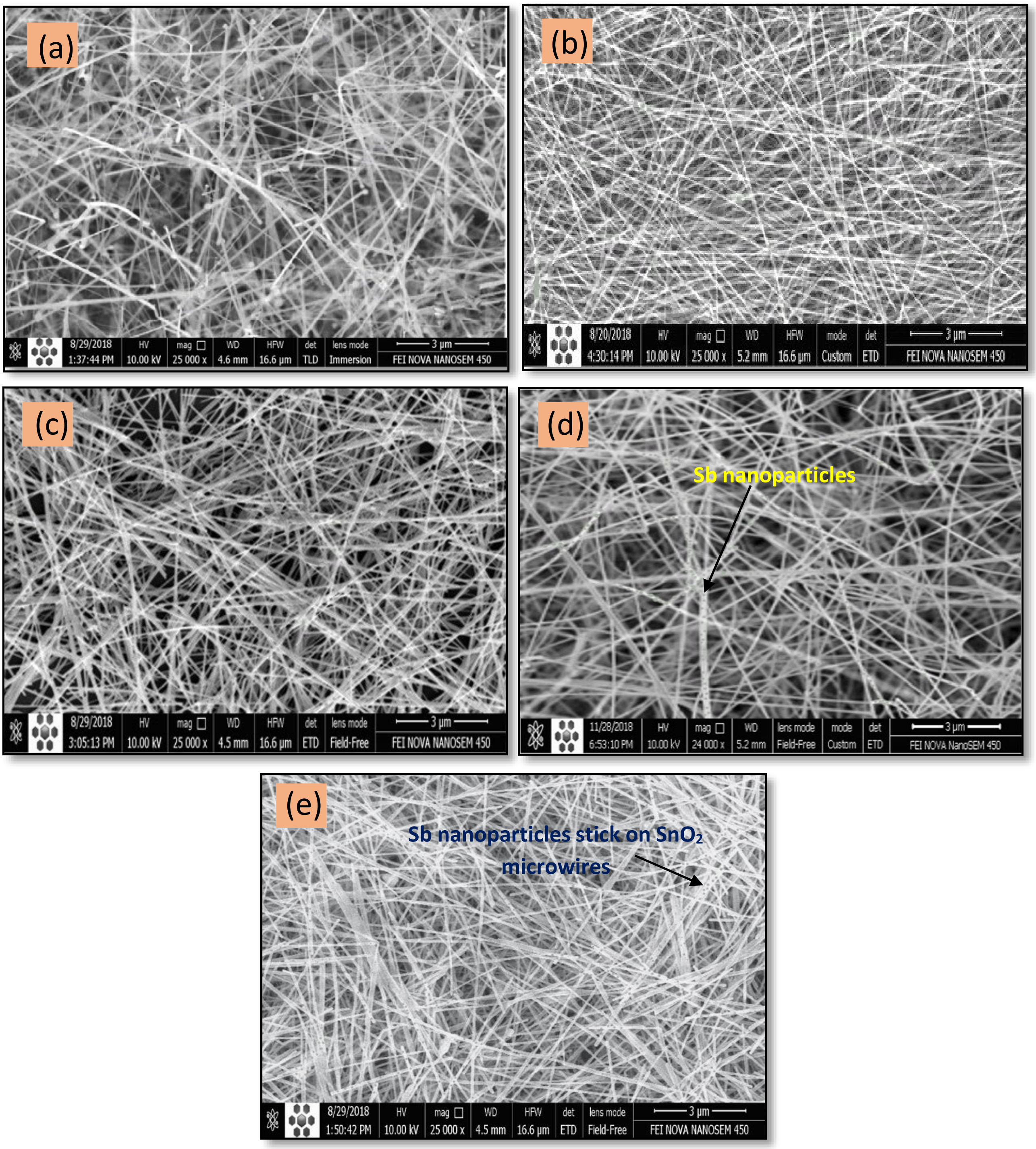

Figure 2 SEM image of (a) pure SnO_2 nanowires, (b) 1% Sb:SnO_2, (c) 3% Sb:SnO_2, (d) 5% Sb: SnO_2, and (e) 7% Sb: SnO_2.

The elemental composition of the films was analyzed using Energy-Dispersive X-ray Spectroscopy (EDX). Figures 3 and 4 present the EDX spectra of pure SnO_2 and 7% Sb-doped SnO_2, respectively. Figure 3 confirms the presence of tin (Sn), oxygen (O), and chlorine (Cl), with no additional elements detected. Upon doping with 7% antimony (Sb), the EDX spectrum in Figure 4 shows the presence of Sb alongside Sn, O, and Cl, confirming successful incorporation of the dopant.

Notably, the introduction of Sb led to a reduction in the relative atomic percentage of Sn by approximately 4%, as shown in Figure 4. This decrease is accompanied by a reduction in the oxygen content from 25% to approximately 20%, indicating an increase in oxygen vacancies. These vacancies are beneficial for sensing applications, as they provide active sites for gas adsorption. The inset tables in Figures 3 and 4 detail the weight percentages of each element, illustrating a decrease in Sn from 72% to 68% and a corresponding reduction in O content, supporting the formation of enhanced oxygen vacancy sites.

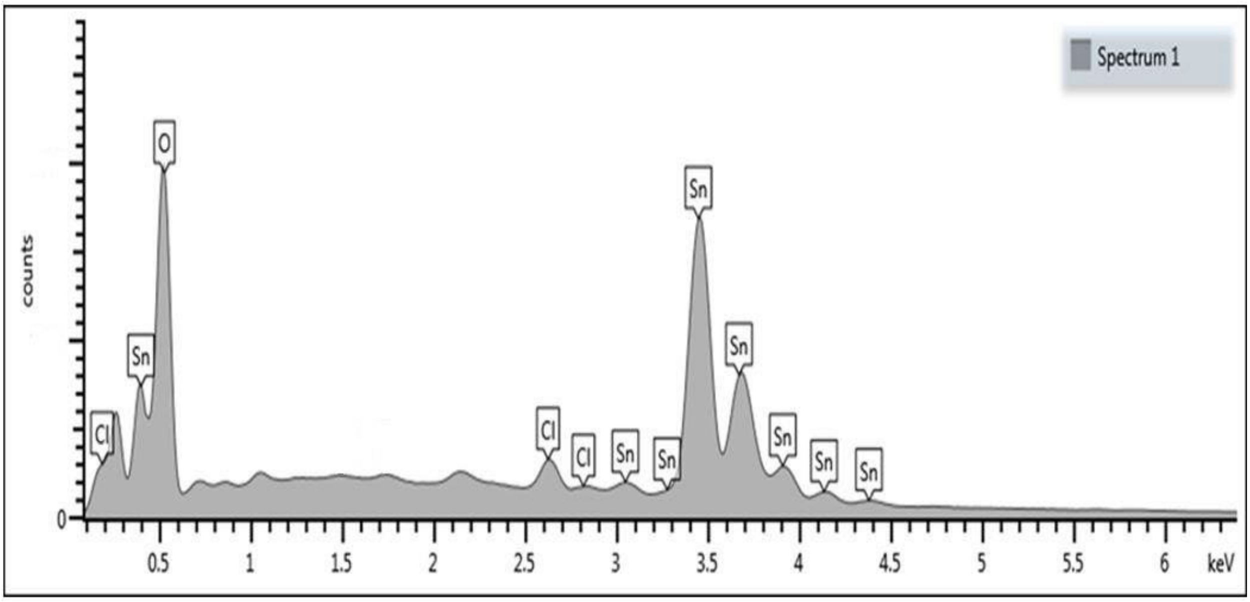

Figure 3 EDX spectrum of as-prepared SnO_2 thin films.

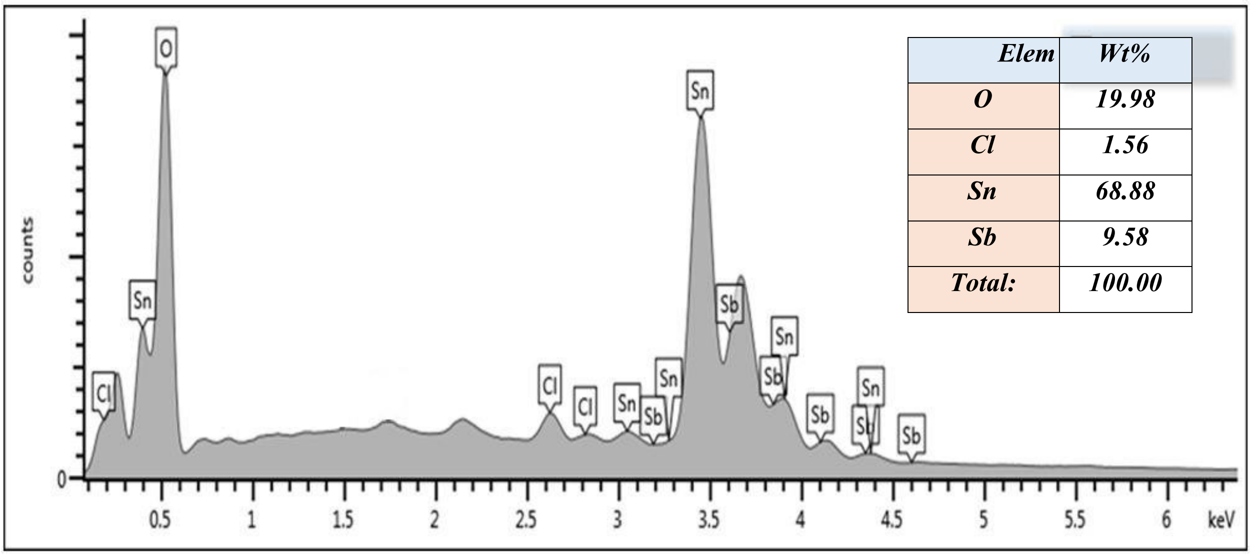

Elem	*Wt%*
O	***19.98***
Cl	***1.56***
Sn	***68.88***
Sb	***9.58***
Total:	***100.00***

Figure 4 EDX spectrum of as-prepared nanowire SnO_2:Sb thin films.

The absorbance spectra of pure SnO_2 and Sb-doped SnO_2 films are presented in Figure 5. As shown, all samples exhibit a gradual increase in absorbance within the wavelength range of 500 to 400 nm, followed by a sharp rise in absorbance at wavelengths below 400 nm. Additionally, it is evident that absorbance increases with higher Sb concentrations. This enhancement may be attributed to increased photon scattering caused by the dopant or to the rise in charge carrier concentration due to Sb doping, which improves the films' conductivity and consequently influences the optical absorption behavior [25, 26].

Furthermore, this trend can be explained by the energy of incident photons. At longer wavelengths (lower photon energy), the photons lack sufficient energy to interact effectively with the material's electrons, allowing light to pass through more readily. In contrast, at shorter wavelengths (higher photon energy), the photons possess enough energy to excite electrons within the material, resulting in increased absorbance.

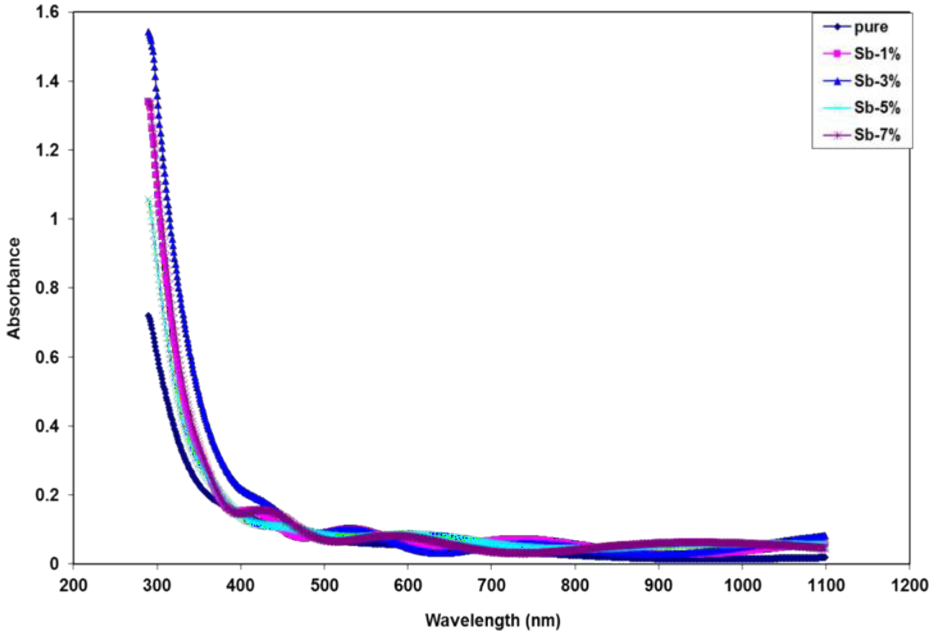

Figure 5 Absorbance as a function of wavelength for pure and Sb doped SnO_2 nanowires.

The energy bandgap of pure and Sb-doped SnO_2 with varying antimony concentrations is illustrated in Figure 6. The figure indicates a direct allowed transition, with the energy bandgap (EgE_g) related to the absorption coefficient (α\alpha) by the Tauc relation [27]:

$$\alpha h\upsilon = B^{'}(h\upsilon - E_g)^{1/2} \tag{1}$$

where $B^{'}$is a constant, $h\upsilon$ is the energy of the photon, and E_g is the energy bandgap.
Figure 6 shows that the energy bandgap of pure SnO_2 nanowires is 3.92 eV. Upon doping with Sb nanoparticles, the bandgap decreases gradually, ranging from 3.92 eV to 3.80 eV as Sb concentration increases from 1% to 3%. This reduction can be attributed to the introduction of donor levels near the conduction band by Sb, which facilitates the absorption of lower-energy photons [28, 29].

Additionally, Figure 7 demonstrates the presence of an indirect bandgap, which also decreases with doping, ranging from 3.07 eV to 3.01 eV. It is observed that the direct bandgap values are consistently higher than those of the indirect bandgap, a trend that aligns well with previous reports in the literature [30].

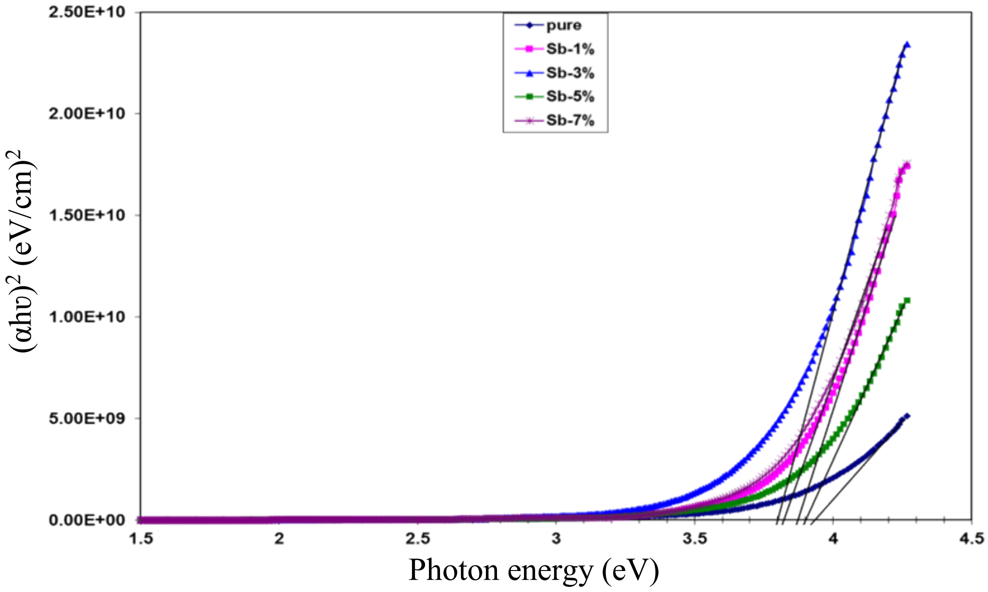

Figure 6 The direct energy band gap of pure and Sb doped SnO_2.

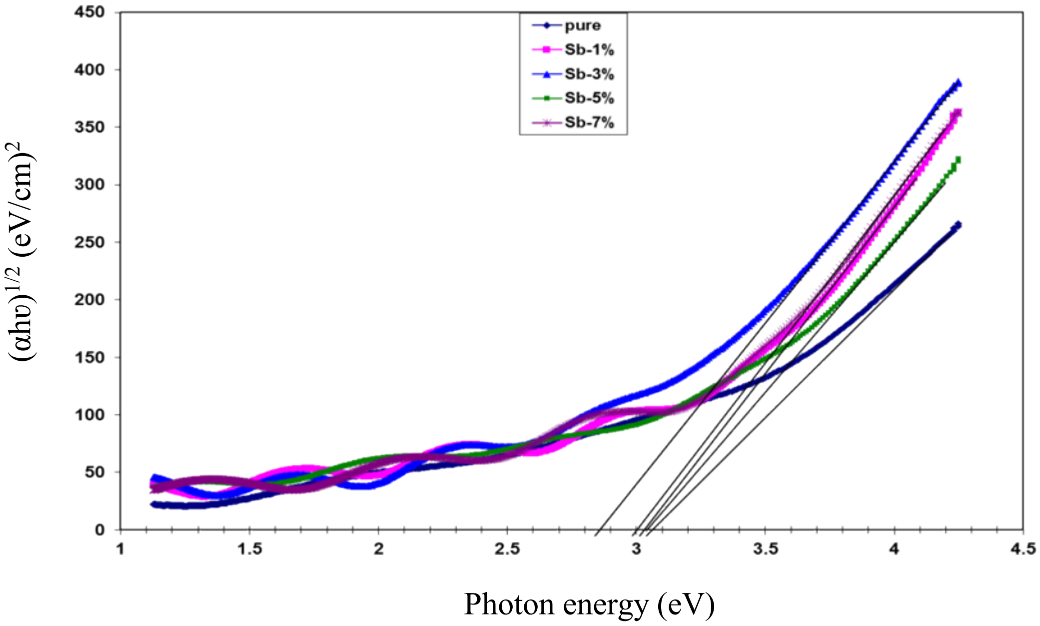

Figure 7 The indirect energy bandgap of pure and Sb doped SnO_2.

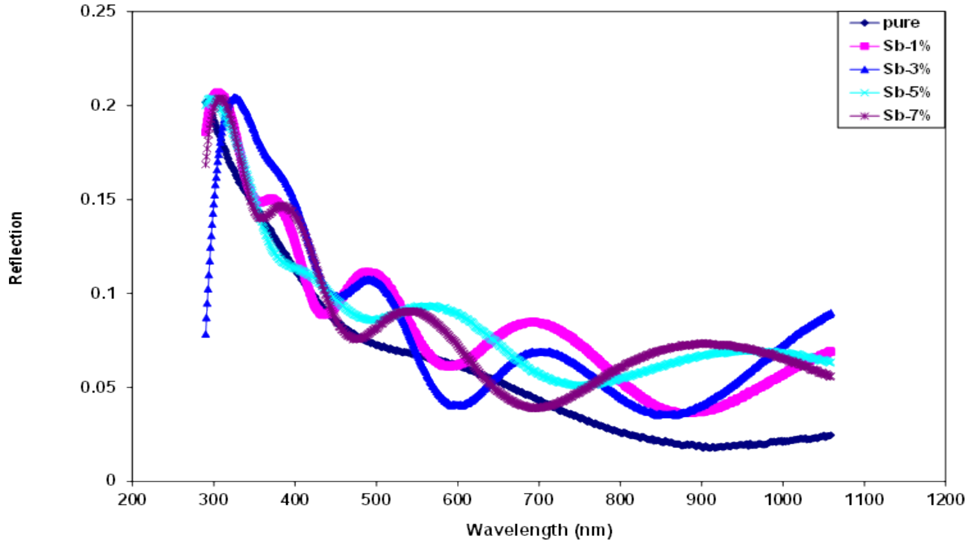

Figure 8 Reflection as a function of wavelength for pure and Sb doped SnO_2 nanowires.

Figure 9 illustrates the variation of the refractive index for pure SnO_2 and Sb-doped SnO_2 films. It is observed that the refractive index decreases slightly from 2.24 to 2.22 with increasing Sb concentration. Additionally, the peak values are shifted toward longer wavelengths. This behavior can be attributed to the reduction in particle size due to the substitution of smaller Sb atoms (atomic radius ~0.62 nm) for larger Sn atoms (atomic radius ~0.69 nm), as well as an increase in charge carrier concentration [33].

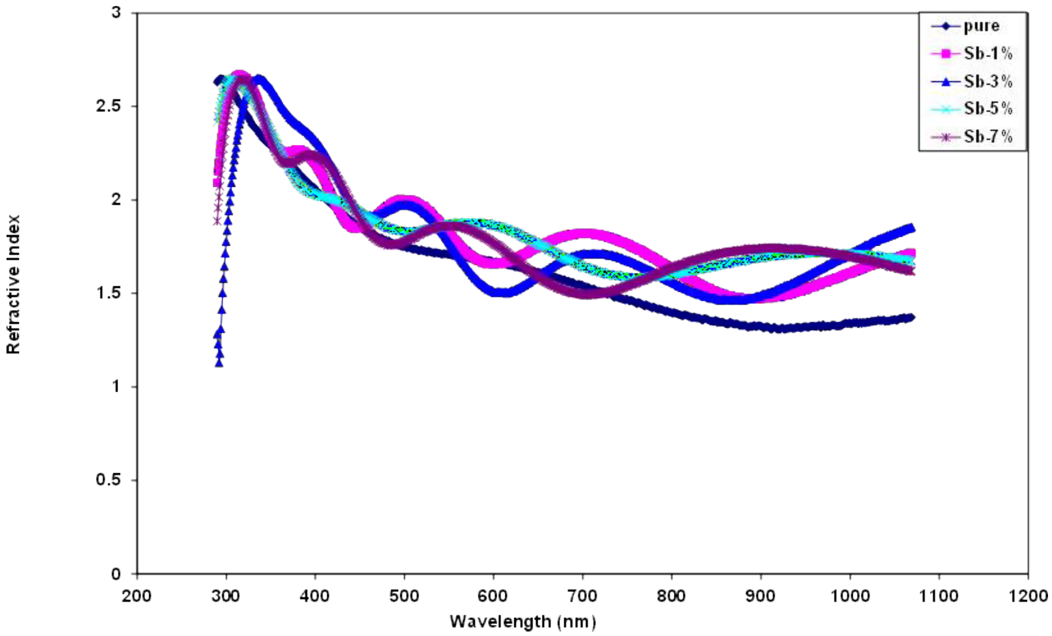

Figure 9 Refractive index as a function of wavelength for un-doped and Sb doped SnO_2 nanowires.

The extinction coefficient is associated with the attenuation of the photon beam as it passes through the film. Figure 10 displays the extinction coefficient (kk) as a function of wavelength for both pure and Sb-doped SnO_2 nanowires. It is evident that the extinction coefficient increases with higher levels of Sb doping. This enhancement can be attributed to increased light scattering caused by the dopant atoms, as well as a rise in the concentration of free charge carriers, which contribute to greater optical absorption [35, 36].

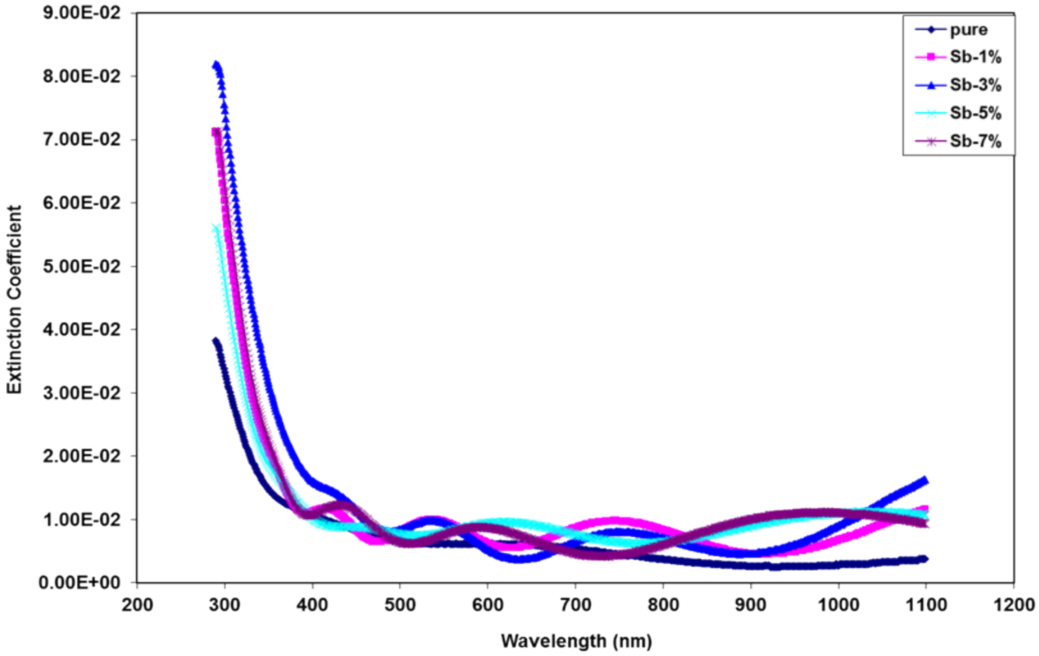

Figure 10 The Extinction coefficient as a function of wavelength for pure and Sb doped SnO_2 nanowires.

These parameters depend on the interaction between electrons and incident photons and are defined by the following equations [37]:

$$\varepsilon_{r} = n^2 - k_e^2 \qquad (2)$$

$$\varepsilon_{i=2nk_{ex}} \qquad (3)$$

Figures 11 and 12 illustrate the variation of the real part of the dielectric constant (εr\varepsilon_r) and the imaginary part of the dielectric constant (εi\varepsilon_i) with wavelength for different Sb concentrations. The real part represents the energy stored within the medium, while the imaginary part corresponds to the energy dissipated. The results show that both the real and imaginary parts of the dielectric constant shift toward longer wavelengths as the Sb concentration increases. Additionally, it is important to note that the real part is consistently higher than the imaginary part. Both the real and imaginary components of the dielectric constant are related to the refractive index and the extinction coefficient. The observed shift of both components toward lower energy with increasing Sb content can be attributed to an enhancement in electron transitions [38].

Table 1 provides a summary comparing this work with previous studies on Sb-doped SnO_2 films prepared by the spray pyrolysis technique, focusing on morphology, crystallite size, and energy bandgap.

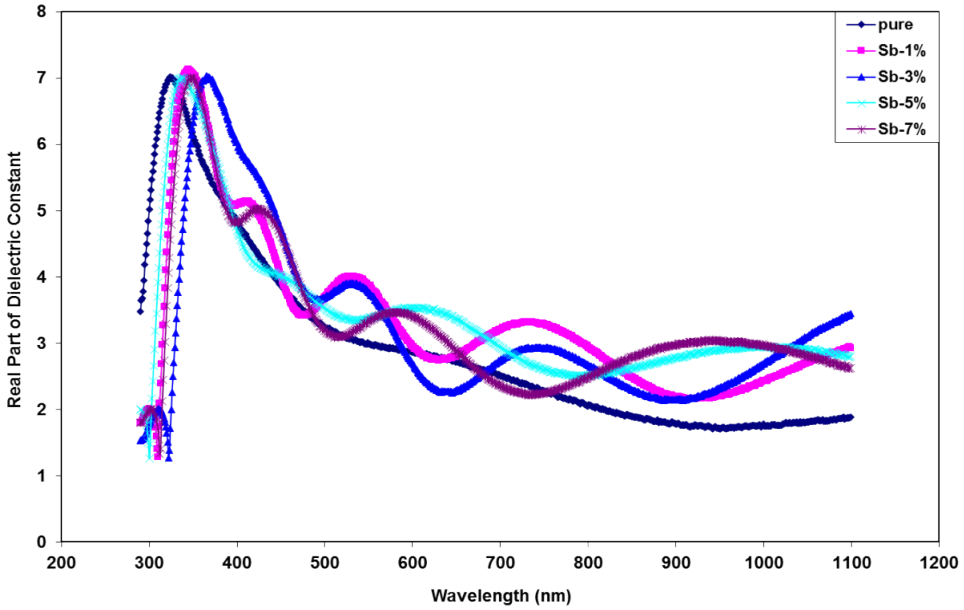

Figure 11 Real part of dielectric constant as a wavelength for pure and Sb doped SnO_2 nanowires.

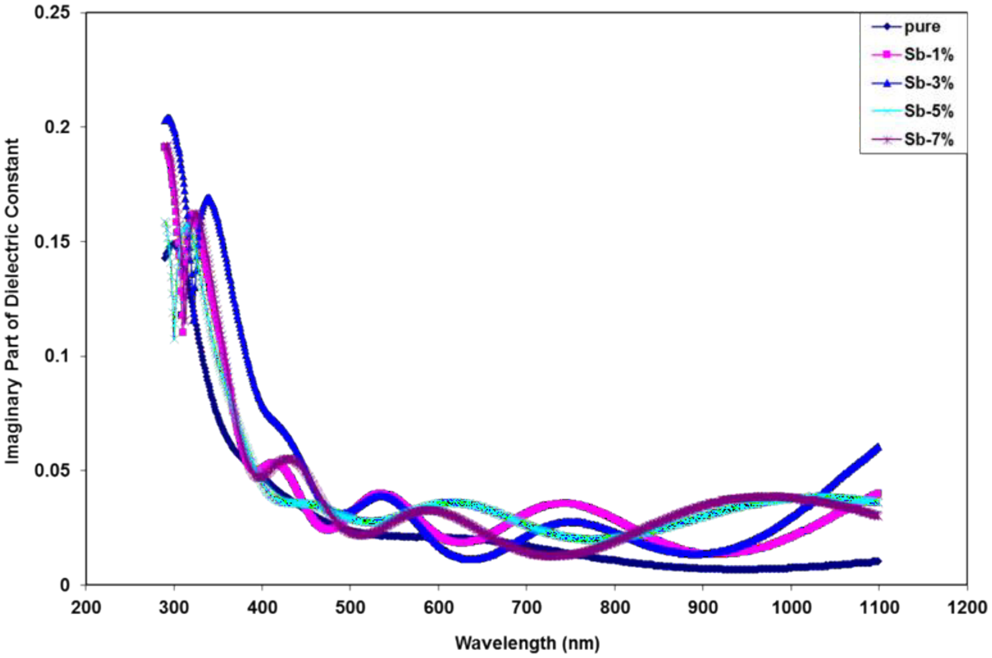

Figure 12 Imaginary part of the dielectric constant as a wavelength for pure and Sb doped SnO_2 nanowires.

Table 1 A comparison with the other previous works of Sb doped SnO_2 prepared by spraypyrolysis technique.

Material	**Solvent**	**Morphology**	**Energy Bandgap (eV)**	**Ref.**
3% $Sb:SnO_2$	2-Propanol	polyhedron	3.72	[39]
5% $Sb:SnO_2$	deionized water and ethylene glycol	polyhedron	3.8	[40]
5% $Sb:SnO_2$	2-propanol and double distilled water	polyhedron	3.16	[41]
6% $Sb:SnO_2$	Ethanol	Mostly spherical and some rod	3.78	[42]
6% $Sb:SnO_2$	$SnCl_2$ dissolved in mixed HCl, distilled water, and methanol. $SbCl_3$ dissolved in isopropyl alcohol	polyhedron	3.95	[43]
3% $Sb:SnO_2$	acetone	SnO_2 nanowires and Sb nanoparticles	3.8	Current work

4. CONCLUSIONS

Pure SnO_2 nanowires and Sb-doped SnO_2 nanowires were synthesized using the spray pyrolysis method, with both structural and optical properties thoroughly investigated. XRD and EDX analyses confirmed the presence of SnO_2 and Sb without any impurities. FESEM analysis revealed the SnO_2 nanowire structure with Sb nanoparticles adhered to the surface of the nanowires. This nanocomposite structure is well-suited for sensing applications. The optical properties demonstrated enhanced absorbance spectra and a tunable energy bandgap with 3% Sb doping. The ability to control the energy bandgap is crucial for photoelectronic applications, making this work particularly promising for detector and sensor devices.

Reference

[1] Habubi, N. F., Ismail, R. A., Hamoudi, W. K., & Abid, H. R. Surface Review and Letters 22 (2015) 1550027
[2] Uysal, B. Ö., & Arıer, Ü. Ö. A. Applied Surface Science 350 (2015) 74
[3] Degler, D., Barz, N., Dettinger, U., Peisert, H., Chasse, T., Weimar, U., Barsan, N. Sensors and Actuators B: Chemical 224 (2016) 256
[4] Mohamed, S. H. Journal of Alloys and Compounds 510 (2012) 119
[5] Yu, S., Li, L., Xu, D., Dong, H., & Jin, Y. Thin Solid Films 562 (2014) 501
[6] Bhardwaj, N., Kuriakose, S., & Mohapatra, S. Journal of Alloys and Compounds 592 (2014) 238
[7] Hussain, N., Zulfiqar, S., Khan, T., Khan, R., Khattak, S. A., Ali, S., & Khan, G. Materials Chemistry and Physics 241 (2020) 122382

[8] Kim, Y. S., Yu, B. K., Kim, D. Y., & Kim, W. B. Solar Energy Materials and Solar Cells 95 (2011) 2874
[9] Hsu, C. L., Chen, K. C., & Hsueh, T. J. IEEE Transactions on Electron Devices 61 (2014) 1347
[10] Mahapatra, A. D., & Basak, D. Sensors and Actuators A: Physical 312 (2020) 112168
[11] Feng, H. T., Zhuo, R. F., Chen, J. T., Yan, D., Feng, J. J., Li, H. J. Physica E: Low-dimensional Systems and Nanostructures 41 (2009) 1640
[12] Fauzia, V., Yusnidar, M. N., Lalasari, L. H., Subhan, A. Journal of Alloys and Compounds 720 (2017) 79
[13] Yang, W., Yu, S., Zhang, Y., & Zhang, W. Thin Solid Films 542 (2013) 285
[14] Deng, H., Kong, J., & Yang, P. Journal of Materials Science 20 (2009) 1078
[15] Gürakar, S., & Serin, T. Materials Research Express 6 (2019) 086423
[16] A. M. Alwan, A. A. Yousif, and H. R. Abed, AIP Conference Proceedings 2190 (2019) 20086
[17] Alwan, A. M., Yousif, A. A., & Wali, L. A. Plasmonics 13 (2018) 1191
[18] Abed, H. R., Alwan, A. M., Yousif, A. A., & Habubi, N. F. Optical and Quantum Electronics 51 (2019) 333
[19] W. Antoine, K. Kennedy, Exp. Theo. NANOTECHNOLOGY 7 (2023) 131
[20] Sun, M., Liu, J., & Dong, B. Current Applied Physics 20 (2020) 462
[21] Chen, A., Xia, S., Ji, Z., Xi, J., Qin, H., & Mao, Q, Surface and Coatings Technology 322 (2017) 120
[22] Singh, M., Goyal, M., & Devlal, K. Journal of Taibah University for Science 12 (2018) 470
[23] Liu, S., Ding, W., Gu, Y., & Chai, W. Physica Scripta 85 (2012) 065601
[24] Ramarajan, R., Kovendhan, M., Thangaraju, K., Joseph, D. P., & Babu, R. R. Applied Surface Science 487 (2019) 1385
[25] Liu, W. W., Liu, C. L., Chen, X. B., Lu, J. H., Chen, H. X., & Miao, Z. Z. Physics Letters A 384 (2020) 126172
[26] Elangovan, E., & Ramamurthi, K. Journal of Experimental and Industrial Crystallography 38 (2003) 779
[27] Mazloom, J., Ghodsi, F. E., & Gholami, M. Journal of Alloys and Compounds 579 (2013) 384
[28] Caglar, Y. Journal of Alloys and Compounds 560 (2013) 181
[29] Muhammad Ismail, Wang Xiangke, Ali H. Reshak, Dania Ali, Aneeba Amjad, Qaisar Khan, Muhammad Ishaq, Abdul Ahad Khan, Zeshan Zada, Exp. Theo. NANOTECHNOLOGY 7 (2023) 95
[30] Abdel-Galil, A., Hussien, M. S., & Yahia, I. S. Superlattices and Microstructures 147 (2020) 106697
[31] Kate, R. S., Bulakhe, S. C., & Deokate, R. J. Optical and Quantum Electronics 51 (2019) 319
[32] Okbi, F., Lakel, S., Benramache, S., & Almi, K. Semiconductors 54 (2020) 58
[33] Yadav, A. A., Pawar, S. C., Patil, D. H., & Ghogare, M. D. Journal of Alloys and Compounds 652 (2015) 145
[34] J. Radehaus, Exp. Theo. NANOTECHNOLOGY 7 (2023) 143
[35] Fadavieslam, M. R. Journal of Materials Science 27 (2016) 4943
[36] Raju, M. J. S., & Bhattacharya, S. S. Materials Today: Proceedings 5 (2018) 10097
[37] Saeedabad, S. H., Selopal, G. S., Rozati, S. M., Tavakoli, Y., & Sberveglieri, G. Journal of Electronic Materials 47 (2018) 5165